Ultrasound Monitoring of In Vitro Radio Frequency Ablation by Echo Decorrelation Imaging

T. Douglas Mast, PhD, Daniel P. Pucke, Swetha E. Subramanian, BTech, William J. Bowlus, Steven M. Rudich, MD, PhD, Joseph F. Buell, MD

Objective. The purpose of this study was to test ultrasound echo decorrelation imaging for mapping and characterization of tissue effects caused by radio frequency ablation (RFA). ***Methods.*** Radio frequency ablation procedures (6-minute duration, 20-W power) were performed on fresh ex vivo bovine liver tissue (n = 9) with continuous acquisition of beam-formed ultrasound echo data from a 7-MHz linear array. Echo data were processed to form B-scan images, echo decorrelation images (related to rapid random changes in echo waveforms), and integrated backscatter images (related to local changes in received echo energy). Echo decorrelation and integrated backscatter values at the location of a low-noise thermocouple were assessed as functions of temperature. Echo decorrelation and integrated backscatter images were directly compared with ablated tissue cross sections and quantitatively evaluated as predictors of tissue ablation and overtreatment. ***Results.*** Echo decorrelation maps corresponded with local tissue temperature and ablation effects. Consistent echo decorrelation increases were observed for temperatures above 75°C, whereas integrated backscatter maps showed a nonmonotonic temperature dependence complicated by acoustic shadowing, with high variance at large temperature elevations. In receiver operating characteristic curve analysis of echo decorrelation and integrated backscatter maps as predictors of local tissue ablation, echo decorrelation performed well (area under the receiver operating characteristic curve [AUROC] = 0.855 for ablation and 0.913 for overtreatment), whereas integrated backscatter performed poorly (AUROC < 0.6). ***Conclusions.*** Echo decorrelation imaging can map tissue changes due to RFA in vitro, with local echo decorrelation corresponding strongly to local tissue temperature elevations and ablation effects. With further development and in vivo validation, echo decorrelation imaging is potentially useful for improved image guidance of clinical RFA procedures. ***Key words:*** echo decorrelation imaging; radio frequency ablation; therapy monitoring; ultrasound temperature measurement.

Abbreviations
AUROC, area under the receiver operating characteristic curve; RFA, radio frequency ablation; ROC, receiver operating characteristic

Received October 22, 2007, from the Departments of Biomedical Engineering (T.D.M., D.P.P., S.E.S., W.J.B.) and Surgery (S.M.R.), University of Cincinnati, Cincinnati, Ohio USA; and Department of Surgery, University of Louisville, Louisville, Kentucky USA (J.F.B.). Revision requested December 17, 2007. Revised manuscript accepted for publication May 8, 2008.

This research was funded by the American Institute of Ultrasound in Medicine Endowment for Education and Research, the University of Cincinnati Cancer Center, and the National Science Foundation grant IIP-0652208, and MIMTeC, and NSF I/UCRC.

Address correspondence to T. Douglas Mast, PhD, Department of Biomedical Engineering, University of Cincinnati, 6168 Medical Sciences Building, 231 Albert Sabin Way, Cincinnati, OH 45267-0586 USA.

E-mail: doug.mast@uc.edu

Interstitial thermal ablation methods, including radio frequency and laser approaches, have recently become important tools for cancer treatment. Available approaches include a number of interstitial ablation devices using radio frequency electromagnetic waves[1] as well as microwave and laser radiation.[2] Monopolar and bipolar radio frequency ablation (RFA) devices are considered the most viable potentially curative treatments for nonresectable liver tumors, including hepatocellular carcinoma and metastases,[3] and are increasingly used for other soft tissue tumors.[4] Ultrasound ablation, including noninvasive high-intensity focused ultrasound[5] as well as minimally invasive bulk ablation,[6] is an alternate modality with considerable promise for clinical applications.

Currently, RFA and other thermal ablation methods are most commonly guided by conventional B-scan ultrasound imaging.[4] B-scans can facilitate accurate tumor localization and probe placement in transabdominal, interstitial,[6] and laparoscopic[7] imaging configurations. Under some conditions, thermal lesions can be identified by locally increased B-scan brightness, as has been shown for high-intensity focused ultrasound ablation.[8,9] However, B-scan imaging provides only limited monitoring of ablation progress, primarily detecting gas generation, which has several causes, including nonthermal cavitation[10] as well as tissue boiling.[11] Although magnetic resonance imaging guidance is a powerful technique that can provide targeting, temperature monitoring, and therapy control,[12,13] use of magnetic resonance imaging guidance for RFA introduces considerable expense and complexity compared with conventional percutaneous or surgical procedures. Thus, improved methods for ultrasound guidance of RFA, as well as for other thermal ablation methods, are needed.

In addition to conventional B-scan imaging, several techniques with potential for ultrasound-based monitoring of RFA and other thermal ablation methods have been tested. These include echo strain imaging for temperature measurement,[14,15] which can potentially provide quantitative temperature estimates but is limited by echo decorrelation effects and tissue motion. Methods that image tissue elasticity changes, such as ultrasound elastography[16,17] and acoustic radiation force impulse imaging,[18] have potential for evaluating the extent of tissue ablation, particularly after thermal treatments. Other potential methods for ultrasound monitoring of RFA include attenuation mapping[19,20] and tissue characterization based on local scattering properties.[20–22] Although all of these methods have shown potential for ultrasound imaging to characterize thermal ablation, their potential for real-time monitoring in RFA procedures is limited because of vapor bubble activity, which occurs consistently, causing large changes in local tissue scattering and attenuation,[16,17] and results in substantial echo decorrelation that can degrade the performance of strain-based temperature and elasticity imaging methods.

B-scans obtained during ablation show apparently random changes in echo signals associated with lesioning, which can be quantified and imaged. The echo changes observed are greatest in hyperechoic regions presumably associated with tissue boiling but can also be observed in isoechoic regions. Possible causes of these signal variations may include gas activity, structural changes due to ablation, and speckle motion due to acoustic streaming, radiation force, and thermal expansion. This phenomenon is similar to large thermally induced fluctuations in Doppler ultrasound signals, which have been qualitatively assessed for monitoring of thermal ablation.[23] Local echo signal fluctuations in B-mode images have previously been quantified by a position-dependent echo difference parameter that can be directly imaged,[24] related to "turbulence" measures used in color Doppler imaging.[25] In this approach, differences between beam-formed echo waveforms from sequential B-scans were squared, spatially filtered, and cumulatively summed over multiple frames to obtain an "echo difference" map, which can then be superimposed on conventional B-scan images. Preliminary results have shown potential for echo difference imaging to image localized tissue ablation both in vitro and in vivo.[24]

In the work presented here, random ultrasound echo changes were quantified by mapping the position-dependent decorrelation between A-scan signals acquired at closely spaced temporal intervals. This approach is related to previous methods for mapping spatially dependent echo decorrelation, which have proven useful for blood velocity estimation,[26] estimation of scan plane motion,[27] verification of speckle-tracking performance,[28] and localization of thermal lesion boundaries.[29] Here, position-dependent signal decorrelation was used to form images depicting areas of rapid echo changes caused by thermal ablation. These decorrelation maps, comprising parametric images that can be superimposed on conventional B-scans, can be used to predict position-dependent tissue coagulation during thermal ablation procedures. This imaging method was tested during controlled in vitro RFA procedures, and the resulting parametric images

were quantitatively compared with the local tissue temperature as well as gross tissue histologic characteristics. The same quantitative comparisons were performed for parametric images of integrated ultrasound backscatter.[20,22] The results show promise for ultrasound decorrelation imaging to detect, map, and characterize thermal ablation effects in the presence of the strong vaporization effects common to RFA.

Materials and Methods

Theory

In the following, methods are given for quantitative imaging of echo decorrelation and related quantities. In this development, the function $p(y,z,t)$ represents a set of analytic A-line signals for a single B-scan image frame obtained at time t. The A-line signal for a given azimuthal coordinate y is obtained by beam forming received echoes along the line (y,z), with the range z defined as $ct/2$, where c is the assumed sound speed, and t is the echo arrival time. Each A-line signal is then Hilbert transformed to obtain a (complex) analytic signal, $p(y,z)$. A conventional B-scan displays the amplitude envelope of this signal, $|p(y,z)|$, usually after logarithmic or other compression.

Computation of spatially averaged parameters, such as integrated backscatter,[30] requires integration of image-related quantities over 2 dimensions after appropriate windowing. For any 2-dimensional function, $f(y,z)$, a spatial average for the position (y,z) is defined by the 2-dimensional integral

$$(1)\quad \langle f(y,z)\rangle = \iint w(y-y_0)\, f(y_0,z_0)\, dy_0\, dz_0 = w(y,z) \otimes f(y,z),$$

where $\langle\cdot\rangle$ denotes spatial integration; $w(y,z)$ is the spatial window used; and $\otimes$ denotes a 2-dimensional spatial convolution. Thus, spatial averaging or integration of the form given by Equation 1 is equivalent to a convolution operation. This convolution can be efficiently implemented for discretely sampled data using either finite impulse response filters or fast Fourier transform computations.[31]

A spatiotemporal correlation function between 2 sequential B-scan frames, acquired at times t and $t+\tau$, is now defined as

$$(2)\quad R(y,z,t,\tau) = \left\langle p(y,z,t)\, p^*(y,z,t+\tau)\right\rangle,$$

where $p^*(y,z)$ is the complex conjugate of the analytic A-line signal $p(y,z)$, and τ is the time interval between the 2 frames. $R(y,z,t,\tau)$ can be interpreted as a non-normalized cross-correlation for zero spatial shift. Similarly, a zero-lag autocorrelation can be defined as

$$(3)\quad R_0(y,z,t) = R(y,z,t,0) = \left\langle \left|p(y,z,t)\right|^2 \right\rangle.$$

Because the zero-lag autocorrelation is equivalent to an integrated or spatially smoothed map of tissue backscatter strength as a function of position, this quantity is related below to the relative "integrated backscatter" IBS(y,z,t).

A normalized decorrelation measure, similar to the "turbulence" quantity introduced by Kasai et al,[25] is then defined as

$$(4)\quad \sigma(y,z,t) \equiv 2\frac{R_0(y,z,t) - \left|R(y,z,t,\tau)\right|}{R_0(y,z,t) + \overline{R_0}(t)},$$

where $\overline{R_0}(t)$ is the spatial mean value of $R_0(y,z,t)$ for the frame obtained at time t, and the frame delay τ is taken to be fixed. Use of the cross-correlation magnitude $|R(y,z,t,\tau)|$ in Equation 4 results in insensitivity to small phase changes between the 2 image frames at times t and $t+\tau$. Thus, the echo decorrelation parameter defined by Equation 4 is not greatly affected by sound speed changes, thermal expansion, or small-scale tissue motion that may occur within the interframe interval τ.

The particular normalization defined by the denominator of Equation 4 was chosen because normalization by $R_0(y,z,t)$ was found to cause artifactually high decorrelations in tissue regions of low echogenicity, whereas normalization by $\overline{R_0}(t)$ caused similar artifacts in regions of high

echogenicity. The normalization used in Equation 4 results in a more uniform decorrelation map throughout images of inhomogeneous tissue with locally varying backscatter and attenuation properties. The resulting echo decorrelation map is zero in regions where the image is unchanged and maximum in regions where local echo changes are greatest.

Finally, because the echo decorrelation map defined by Equation 4 also varies randomly in time, temporal smoothing can also be used to provide a better estimate of local tissue changes. A temporal smoothing method suitable for real-time implementation is the running average:

$$(5)\quad \bar{\sigma}(y,z,t_i) \equiv (1-\varepsilon)\bar{\sigma}(y,z,t_{i-1}) + \varepsilon\sigma(y,z,t_i),$$

where t_i is the time of the current (ith) echo decorrelation image frame, and ε is a user-defined parameter ($0 < \varepsilon < 1$) that determines the effective length of temporal integration.

Imaging Implementation

The above method for decorrelation imaging has been implemented for ultrasound image data obtained during RFA experiments. B-scan imaging was performed using the 192-element, 7-MHz linear imaging array shown in Figure 1A (L7; Guided Therapy Systems, LLC, Mesa, AZ) controlled by an Iris imaging and ablation system (Guided Therapy Systems). The Iris system provides B-scan imaging with capabilities comparable to clinical diagnostic scanners and direct access to beam-formed A-line signals, as well as user-programmable control of therapeutic ultrasound exposures for image ablate arrays.[6,32] The B-scan gain and time-gain compensation were adjusted to obtain signal levels appropriate for digitization as well as uniform speckle brightness within the liver specimen image. A representative tissue B-scan from the system is shown in Figure 1B.

Beam-formed, megahertz-range A-line signals were recorded from the Iris system using a 14-bit personal computer–based analog-to-digital card (CompuScope CS 14200; Gage Applied Technologies, Montreal, Quebec, Canada) at a sampling rate of 33.3 MHz. In each signal acquisition, 384 A-lines of a 1320-sample length were recorded to disk, comprising 2 entire temporally adjacent B-scan frames with dimensions of 42.2 mm in the array direction and 30.5 mm in the depth direction. The 2 frames recorded in each acquisition consisted of 192 A-lines each, separated by a temporal interval of 19.6 milliseconds (inverse of the system frame rate, 51 Hz). These 2-frame acquisitions were performed at time-stamped intervals separated by 1.27 ± 0.08 seconds (measured mean ± SD, dependent on disk access times).

Recorded echo signals (ie, beam-formed megahertz-range A-lines) were processed in MATLAB (The MathWorks, Natick, MA) to form B-scan images and decorrelation maps. To reduce electromagnetic interference caused by the RFA probe, echo signals were filtered by a Gaussian bandpass filter with a center frequency of 7.36 MHz and a –6-dB bandwidth of 2.35 MHz, applied after zero padding the 1320-sample A-line signals to 2048 samples. This filter also acted as a Hilbert transformer, resulting in complex analytic signals for each beam-formed A-line. B-scan images were computed for display by logarithmically scaling the analytic echo signal amplitudes (A-line envelopes), $|p(y,z,t)|$, with a 60-dB dynamic range.

Echo decorrelation images, $\sigma(y,z,t)$, were computed from temporally adjacent (separated by 19.6 milliseconds, as described above) frames of echo data using a discrete implementation of Equation 4. Spatial correlation functions, R, and autocorrelation functions, R_0, were computed using Equations 2 and 3, respectively. Spatial integration for these computations was performed using a discrete implementation of Equation 1 with the isotropic Gaussian window:

$$(6)\quad w(y,z) = e^{-(y^2+z^2)/(2\gamma^2)},$$

where the length scale, γ, was taken to be 3.5 mm. Running averages for both autocorrelation and decorrelation functions were computed from sequences of echo decorrelation frames (obtained at intervals of 1.27 ± 0.08 seconds) using Equation 5 with the temporal averaging parameter $\varepsilon = 0.05$.

To obtain composite decorrelation/B-scan images, decorrelation maps were logarithmically scaled with a maximum displayed value of $4 \cdot 10^{-2}$ and a minimum displayed value of $4 \cdot 10^{-4}$. Decorrelation values below the displayed minimum were not plotted, whereas values greater than the displayed maximum were plotted equivalently to the maximum displayed value. Composite images were then constructed from hue, saturation, and brightness channels, with hue and saturation for each pixel given by the local scaled decorrelation value and brightness given by the local B-scan amplitude. The resulting composite image shows the entire B-scan with a translucent overlay of the decorrelation map. Decorrelation values below the displayed minimum are invisible, whereas values at or above the displayed maximum appear saturated red. Intermediate decorrelation values range from weakly saturated green through increasingly saturated blue, violet, and red.

For comparison, integrated backscatter images were obtained from a discrete implementation of Equation 3 using echo data and spatial filtering methods identical to those used in the decorrelation images. To isolate any backscatter changes associated with the RFA treatment, integrated backscatter was defined here by the relative position-dependent increase in echo energy, measured in decibels; ie,

$$\text{IBS}(y,z,t) \equiv 10 \cdot \log_{10}\left(\frac{R_0(y,z,t)}{R_0(y,z,0)}\right), \quad (7)$$

where $R_0(y,z,0)$ is the autocorrelation defined by Equation 3, measured before the ablation treatment. The result is a spatially smoothed map of local changes in echo energy caused by RFA. These maps were superimposed on B-scan images in a manner similar to the decorrelation maps described above. Relative integrated backscatter was shown in these composite images with a minimum displayed value of 0 dB and a maximum displayed value of 6 dB.

Experiments

To test the potential of our decorrelation imaging methods for monitoring of RFA, ex vivo liver tissue was ablated in vitro with simultaneous ultrasound imaging. Ultrasound image data were acquired during all experiments as described above. The experimental setup is illustrated in Figure 1. Fresh liver tissue was obtained from a local slaughterhouse, stored in ice at 0°C, and used within 12 hours postmortem. Immediately before each trial, a tissue sample was cut to dimensions of 8.5 × 8.5 × 6 cm and placed in an acrylic cuvette of identical dimensions, with the liver capsule facing upward through the cuvette opening.

A 192-element, 7-MHz linear ultrasound array (L7; Guided Therapy Systems) was placed vertically at one of the vertical cuvette edges, in contact with an acoustically transparent membrane

Figure 1. Setup for in vitro ablation and imaging experiments. **A**, Experimental configuration used in all RFA trials. **B**, B-scan from the Iris system (trial 5, before treatment) showing the inserted RFA probe shaft and thermocouple.

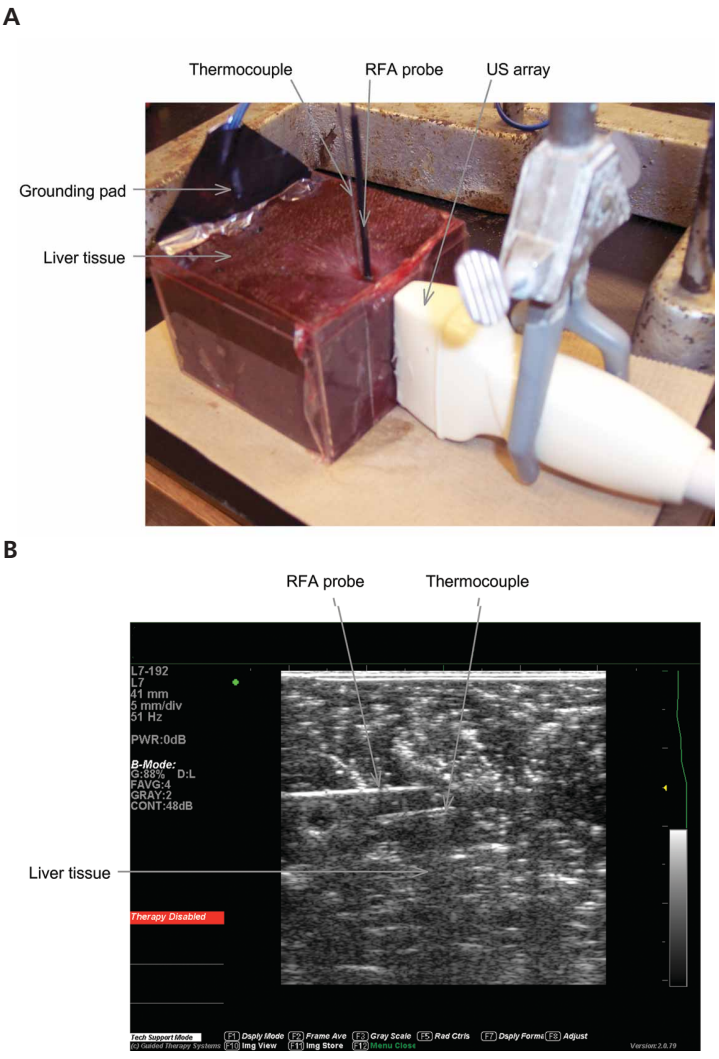

(Tegaderm; 3M, St Paul, MN) that spanned a side window with dimensions of 4 × 6 cm. A foil grounding pad with dimensions of 8.5 × 6 cm, constructed by modifying a clinical grounding pad (PolyHesive E7506; Valleylab, Boulder, CO), spanned the distal tissue surface. Phosphate-buffered saline was added to fill any voids, after which the tissue was manually manipulated to remove any air pockets or large bubbles. A 2-cm RFA probe (LeVeen 2.0 needle electrode; Boston Scientific Corporation, Boston, MA) was inserted through the top tissue surface, approximately parallel to the ultrasound image plane, at a distance of 1.41 ± 0.17 cm from the imaging array, and its tines were deployed within the image plane.

A low-noise, 1-mm-diameter type K thermocouple (GKMQSS-040U-6; Omega Engineering, Inc, Stamford, CT) was inserted slightly distal to the RFA probe shaft at a depth of 1.82 ± 0.24 cm, approximately parallel to the ultrasound image plane, with the active tip placed near the center of the ablated zone. Use of this ungrounded thermocouple was found to reduce variations in the measured temperature caused by electromagnetic interference from the RFA probe. Vertical and horizontal positions of the thermocouple tip were measured on the Iris B-scan image and recorded for each ablation experiment. Measured temperatures were recorded using a digital data logger (Omegaette HH306; Omega Engineering) at a sampling rate of 1 Hz throughout each experiment.

For each ablation procedure, the 2-cm RFA probe was driven by an RFA generator unit (RF 2000B; RadioTherapeutics Corporation, Mountain View, CA) for 6 minutes with an initial power setting of 20 W. Beam-formed echo waveform data from the 7-MHz linear array and temperature data from the low-noise thermocouple were acquired and stored throughout each experiment as described above. This procedure was repeated for 9 trials on separate specimens of fresh bovine liver tissue.

After each ablation trial, a tubular plastic marker was inserted in the track of the RFA probe needle for later identification. Tissue was frozen at –80°C in an acrylic cuvette with dimensions of 8.5 × 8.5 × 6 cm, which maintained the tissue shape and orientation used during the ablation and imaging procedures. Frozen tissue samples were sectioned into calibrated macroscopic slices of 2 mm thickness, cut parallel to the ultrasound image plane, for quantitative evaluation.[6] The tissue cross section corresponding most closely to the image plane was identified by localizing the plastic tube marking the RFA probe track. Regions ablated in each tissue section were histologically quantified by manual image segmentation based on gross discoloration[6] (ImageJ; National Institutes of Health, Bethesda, MD). On the basis of pathologic analysis of in vivo thermal ablation studies, gross discoloration of tissue by thermal effects consistently indicates coagulative necrosis and tissue death.[33] The total volumes of tissue ablation (all coagulated tissue, identified by substantial gross discoloration) were thus estimated and used to compute volumetric ablation rates (milliliters per minute) for each experiment. Similarly, the total volumes of overtreatment (indicated grossly by brown, dehydrated tissue) were determined and used to compute volumetric overtreatment rates for each experiment. Measured volumetric rates for the 9 trials were 1.63 ± 0.4 mL/min for ablation and 0.19 ± 0.11 mL/min for overtreatment.

Data Analysis

For quantitative comparison of echo decorrelation and integrated backscatter with the tissue temperature, these image-based quantities were interpolated to coincide with the thermocouple temperature measurements. Both log-scaled echo decorrelation and decibel-scaled integrated backscatter, computed as described above, were bilinearly interpolated to the corresponding thermocouple location measured from the pre-exposure B-scan for each experiment. The resulting temporal echo decorrelation and integrated backscatter signals were linearly interpolated to synchronize with the thermocouple measurements. The thermocouple-measured temperature, logarithmically scaled echo decorrelation, and decibel-scaled integrated backscatter at the thermocouple location were then analyzed for epochs throughout the treatment duration, ranging from 0 to 6 minutes with a step of 1 second. At each of these instants, the mean and SD for each of these 3 parameters was computed across all trials (n = 9).

To assess possible relationships between the imaged parameters and local tissue temperature, measured epochs were classified into 21 bins according to the thermocouple-measured temperature at each epoch. These bins had center temperatures equally spaced between 25°C and 105°C and widths of 4°C. Mean and SD values of the logarithmically scaled echo decorrelation and decibel-scaled integrated backscatter were computed for the measured epochs within each bin. The number of measurements within each of these bins was between 39 and 246.

For direct comparison between parametric images and ablation effects, segmented tissue cross sections for the image plane in each experiment were cropped to match the region imaged in each corresponding B-scan. Registration of ultrasound and photographic images was performed manually, using clearly imaged spatial reference points such as the RFA probe track and large vessels. Regions of ablation and overtreatment for this registered tissue cross section were manually segmented as described above.

To quantitatively compare locally imaged parameters with local ablation effects at all imaged points, decorrelation and integrated backscatter maps were spatially interpolated to the same spatial grids covered by each photographic tissue cross section. Binary images of tissue ablation for ablated and overtreated zones were formed by classifying the regions inside and outside each segmented zone. Corresponding binary images were obtained for the parameter maps by classifying regions with values above and below a specified threshold. For example, all spatial points with echo decorrelation above a value σ_{thresh} could be predicted to incur ablation. By varying this threshold, as shown below for these experiments, predictions of ablation effects can be made from parameter maps with varying sensitivity and specificity.

The predictive accuracy of the parametric imaging methods was assessed by varying threshold values of echo decorrelation and integrated backscatter and testing the relationship between predictions and observed ablation at all spatial points in each tissue cross section. For a given threshold, each spatial point was counted as a true-positive, true-negative, false-positive, or false-negative prediction for both the echo decorrelation and integrated backscatter maps. Receiver operating characteristic (ROC) curves were obtained by plotting the true-positive versus false-positive prediction rate for both echo decorrelation and integrated backscatter as predictors of both ablation and overtreatment over a range of thresholds spanning the measured range of each parameter.

Results

Figure 2 shows composite ultrasound images for 3 representative trials, together with segmented tissue cross sections spanning each ultrasound

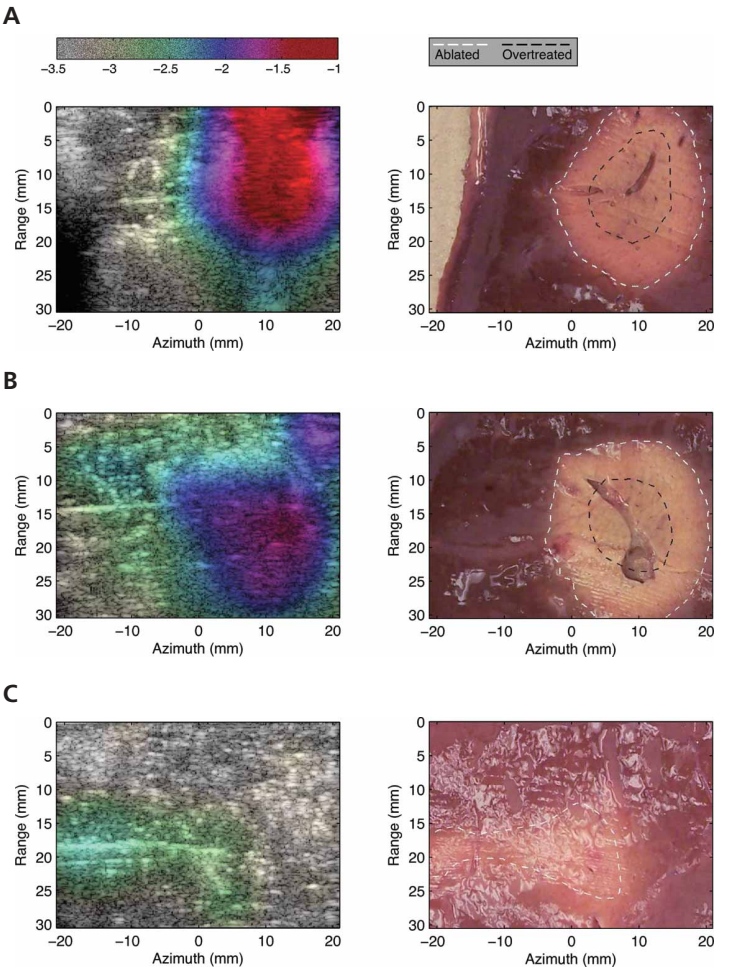

Figure 2. Composite echo decorrelation/B-scan images (left panels) and tissue cross sections (right panels) for 3 of 9 RFA trials. The log-scaled temporal maximum echo decorrelation for each spatial position, $\log_{10}[\bar{\sigma}_{max}(y,z)]$, is presented using the given color map, superimposed on a postablation B-scan image with a 60-dB dynamic range. Tissue cross sections correspond to the ultrasound image plane, with boundaries of the overall ablated zone marked by dashed white lines and boundaries of the inner overtreated region marked by dashed black lines. **A**, Trial 1. **B**, Trial 5. **C**, Trial 7.

image plane. Composite echo decorrelation/B-scan images, formed as described in "Materials and Methods," are shown in the left panels. The B-scans used were obtained after 6 minutes of RFA (ie, at the end of the treatment), whereas the depicted decorrelation maps show the maximum decorrelation value incurred at each image point throughout the treatment. Log-scaled decorrelation maps, $\log_{10}[\sigma_{max}(y,z)]$, are displayed using the scale shown by the color bars of Figure 2. Corresponding registered tissue cross sections, with the segmented boundaries of ablated and overtreated regions, are shown in the right panels of Figure 2. Spatial correspondence between echo decorrelation and tissue ablation is fairly consistent among the trials, with good qualitative agreement between elevated echo decorrelation and observable ablation effects. Notably, regions of overtreatment correspond spatially to regions of high echo decorrelation, whereas trial 7, in which no overtreatment was observed, also shows a smaller overall echo decorrelation. Quantitative testing of this spatial correspondence is given below.

For comparison, corresponding composite integrated backscatter/B-scan images are shown in Figure 3. The left panels of Figure 3 show decibel-scaled temporal maximum values of the relative integrated backscatter for each image point, merged with the same B-scan image data as in Figure 2. The same B-scans are shown with a 60-dB dynamic range in the right panels of Figure 3. Comparison of integrated backscatter or B-scan images with the ablated tissue cross sections from Figure 2 indicates poor correspondence of observable changes in echo energy with local tissue ablation. Consistent with this observation, the quantitative analysis given below shows that echo decorrelation performs more accurately, as a predictor of local tissue ablation in the reported experiments, than integrated backscatter.

Average temperature, echo decorrelation, and integrated backscatter at the thermocouple tip are plotted in Figure 4 as a function of exposure time, including the mean and SD among the 9 trials. The time-dependent temperature rise follows a pattern typical for thermal ablation by steady heat sources.[34] Both echo decorrelation and integrated backscatter show a tendency to increase in both the mean and SD throughout each treatment. However, the small variance of integrated backscatter at small treatment times results from the relative definition of integrated backscatter used here (Equation 7), by which the relative integrated backscatter is always 0 dB at the onset of treatment ($t = 0$). Notably, although all 3 measured quantities are seen to increase similarly with time, this behavior does not imply similar correlation between all 3 quantities.

To directly observe correspondence between measured echo decorrelation or integrated backscatter and measured temperature, these 2 image-derived quantities can be depicted as functions of tissue temperature. To achieve this, all measured epochs from the 9 ablation experiments were classified into temperature bands as described in "Materials and Methods." Echo decorrelation and integrated backscatter for epochs within each of these specified temperature bands are plotted as mean and SD in Figure 5. These plots show a marked difference between the 2 measured parameters. Echo decorrelation shows a tendency to remain roughly constant up to temperatures of about 75°C and to rise with further temperature increases. Variance of the logarithmically scaled echo decorrelation is roughly constant throughout the measured temperature ranges. In contrast, the decibel-scaled integrated backscatter shows a more complicated, nonmonotonic relationship between temperature and backscatter, with large variance at temperatures between about 70°C and 85°C and relatively small values for temperatures above 100°C. The observed small values for integrated backscatter at temperatures above 80°C may be due to acoustic shadowing caused by vapor formation.[4,34] Measured ROC curves for prediction of ablation and overtreatment from echo decorrelation and integrated backscatter are shown in Figure 6. These curves show that, for the experimental conditions used here, echo decorrelation is much more accurate than integrated backscatter as a predictor of local ablation effects. As judged by the area under the receiver operating characteristic curve (AUROC), echo decorrelation also shows better success as a predictor of overtreatment (AUROC = 0.913) than as a predictor of overall ablation (AUROC = 0.855). Corresponding AUROC values for integrated backscatter were 0.5925 for ablation and 0.5758

for overtreatment. On the basis of the measured ROC curves, optimal thresholds for echo decorrelation in these experiments can be estimated as the farthest points from the diagonal. The resulting threshold values are $2.9 \cdot 10^{-3}$ for ablation and $5.6 \cdot 10^{-3}$ for overtreatment. As with any classifier, choice of threshold allows a user to adjust the sensitivity and specificity of echo decorrelation as a predictor of local ablation.

Discussion

The echo decorrelation imaging method introduced here has the potential to indicate the spatial extent of tissue ablation in real time. Echo decorrelation maps may provide an indication of any incompletely ablated target regions, such as in the vicinity of a large blood vessel. Because failure to ablate all malignant cells can cause tumor recurrence, this capability could greatly improve image guidance for RFA. The potential utility of echo decorrelation imaging for ablation monitoring and possible limitations on its use are discussed below.

The physical mechanisms causing the mapped echo decorrelation are not fully understood. One likely contributor is activity of vapor bubbles caused by tissue heating to temperatures approaching or exceeding 100°C. Such vapor bubbles may incur violent, random motion that can be detected as audible sound.[8,35,36] Any such fluctuations likely cause substantial decorrelation of echo signals emanating from the heated region. If ultrasonic ablation, such as high-intensity focused ultrasound[5] or interstitial intense ultrasound,[6] is used instead of RFA, acoustic cavitation induced by the therapeutic sonication is another potential source of echo decorrelation. In addition, the microstructure of tissue changes substantially during thermal ablation as the tissue coagulates due to heat-induced effects such as protein denaturation, cell rupture, and tissue cracking. These structural changes are other possible sources for decorrelation of sequentially acquired echo signals from a given tissue region.

Comparisons between measured echo decorrelation and tissue temperature, shown in Figure 5A, suggest that echo decorrelation may be useful for detection of local temperature elevations to 75°C and above. A possible explanation is that the effects causing echo decorrelation, such as bubble activity and tissue structural changes, may increase to measurable levels as the tissue temperature exceeds this apparent threshold. Because clinical RFA typically induces tissue temperatures exceeding 100°C,[1] consistent with temperatures measured here in vitro, this temperature sensitivity suggests that echo decorrelation imaging should be useful for confirmation of successful ablation.

Unlike echo strain imaging methods,[14,15] which depict local dilatations of echo waveforms, echo decorrelation imaging does not directly depict thermal expansion or sound speed changes resulting from temperature elevations. Because

Figure 3. Composite integrated backscatter/B-scan images (left panels) and corresponding B-scans (right panels) for 3 of 9 RFA trials. The decibel-scaled temporal maximum integrated backscatter for each spatial position is presented using the given color map, superimposed on the same post-RFA B-scan images. B-scans obtained at 6 minutes of RFA treatment for each trial are displayed using a 60-dB dynamic range. **A**, Trial 1. **B**, Trial 5. **C**, Trial 7.

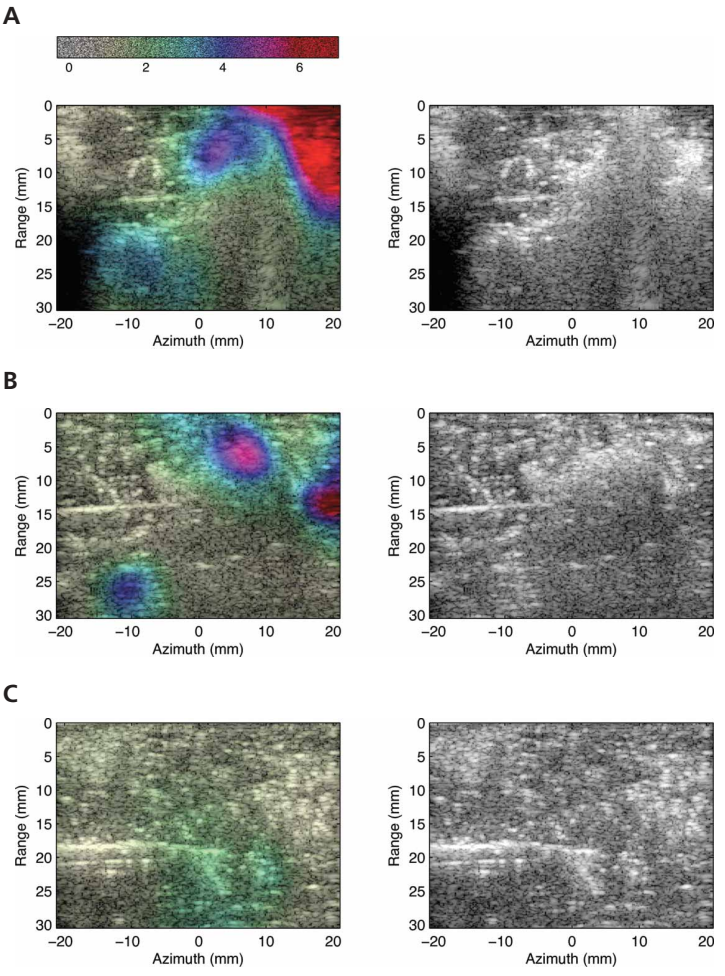

decorrelations were computed between echoes separated by only 19.6 milliseconds, the small temperature elevations incurred over this interval (≈0.01°C) cause negligibly small thermal expansion and sound speed changes. In addition, the echo decorrelation parameter used here is insensitive to small signal phase changes associated with sound speed changes and thermal expansion. For this reason, measured echo decorrelation parameters generally remained small for subablative temperatures below about 75°C, even though the tissue temperature rose most rapidly in this range, as shown in Figure 4.

Although some previous studies have shown a link between elevations in tissue temperature and backscattered echo energy,[20–22] the experimental results reported here suggest that echo decorrelation imaging is more successful than integrated backscatter imaging as a predictor of tissue temperature and thermal coagulation effects caused by RFA. Although both echo decorrelation and backscatter may increase in

Figure 4. Mean and SD of measured parameters at the thermocouple position as a function of treatment time for 9 RFA experiments. The mean of each parameter is shown as a solid line, whereas the dashed lines are drawn 1 SD above and below the mean. **A**, Temperature. **B**, Log-scaled echo decorrelation, $\log_{10}[\sigma(y,z,t)]$. **C**, Decibel-scaled integrated backscatter.

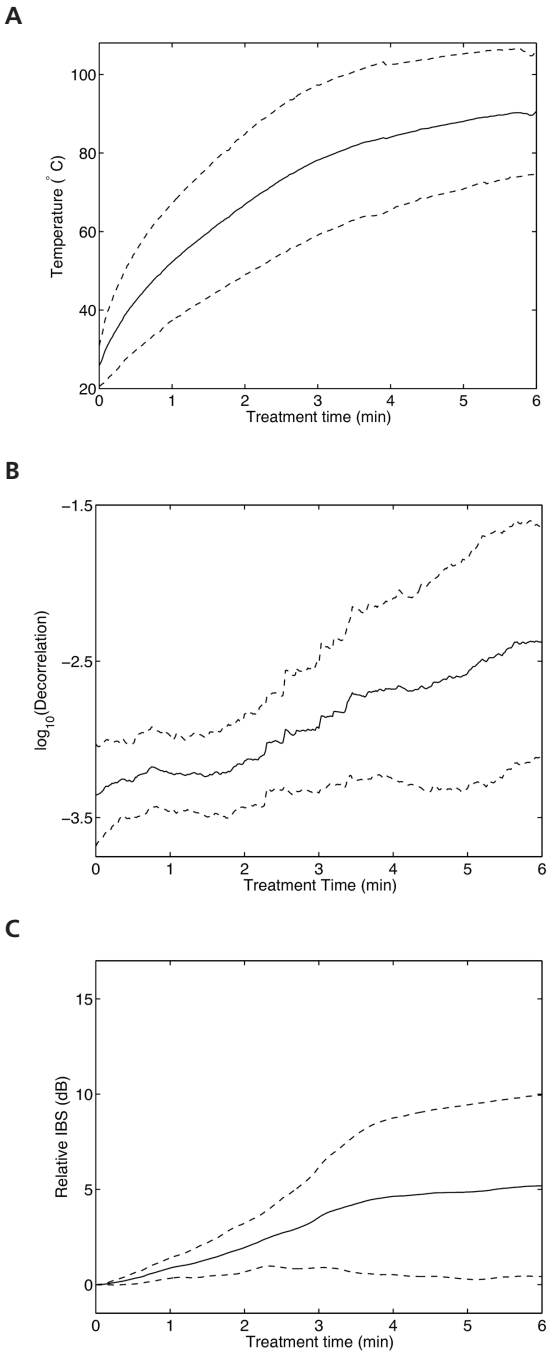

Figure 5. Mean and SD of imaged parameters at the thermocouple position for all simultaneous temperatures within 4°C bands centered at temperatures between 25°C and 105°C. **A**, Log-scaled echo decorrelation. **B**, Decibel-scaled integrated backscatter.

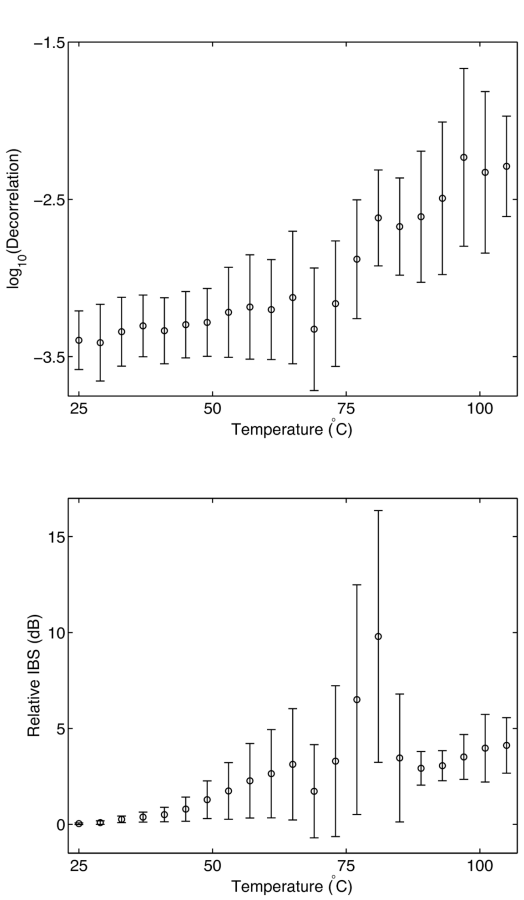

the presence of violent vapor bubble activity, measurements of heating-induced backscatter changes are complicated by acoustic shadowing, associated with vapor bubbles as well as increased attenuation of thermally coagulated tissue.[20,37] In RFA, in which a large tissue volume is ablated at once, such shadowing can cause ultrasound echo energy to decrease over portions of the heated region, countering the amplitude changes monitored by integrated backscatter imaging.

In contrast, echo decorrelation imaging maps a normalized measure of relative echo waveform changes as defined by Equation 4. Because these waveform changes are scaled according to the spatially averaged waveform energy, echo decorrelation imaging is less sensitive to signal amplitude changes caused by acoustic shadowing effects. The results presented here confirm that echo decorrelation can map tissue ablation over large spatial regions, including regions affected by acoustic shadowing.

Figure 6. Receiver operating characteristic curves for accuracy of locally predicted tissue ablation and overtreatment at all points within the image plane. The true-positive (TP) prediction rate is plotted versus the false-positive (FP) prediction rate for varying thresholds of the imaged decorrelation and integrated backscatter parameters. **A**, Prediction based on echo decorrelation maps. **B**, Prediction based on integrated backscatter maps.

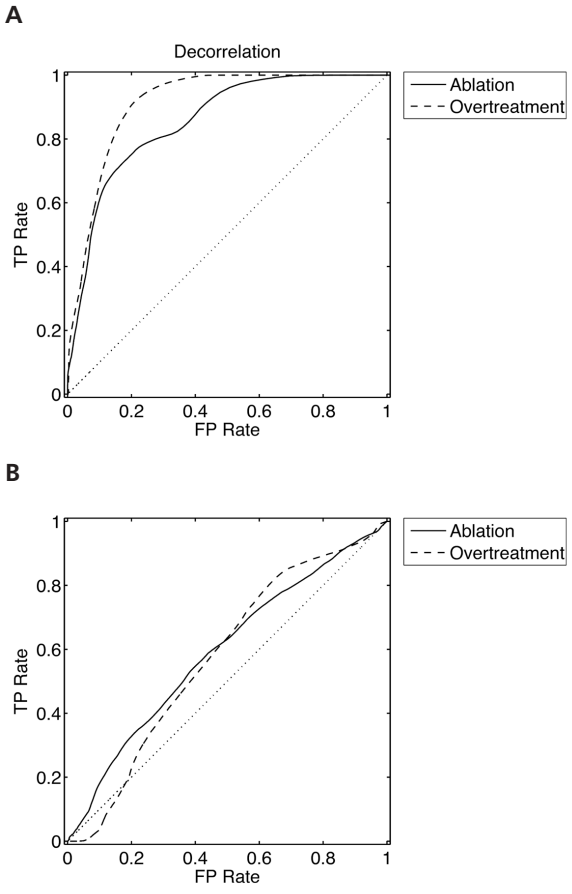

The ROC curves shown in Figure 6 indicate that decorrelation imaging can predict regions incurring thermal ablation, with predictive accuracy substantially exceeding that for integrated backscatter imaging. Echo decorrelation imaging shows even greater accuracy in locally predicting tissue overtreatment (ie, heating of tissue considerably beyond its thermal ablation point, as in the brown cores of severe RFA-induced thermal lesions). This ability to confirm and spatially map severe tissue ablation may be useful in monitoring of RFA and other thermal ablation methods because overtreatment of a specific tissue region (eg, at the center of the heated volume) may be useful as a clinical end point.

Notably, the relative magnitude of the echo decorrelation depends on several factors, including the spatial averaging used, the imaging frame rate, and the beam patterns of the imaging transducer used, in addition to the tissue heating and ablation effects being monitored. Thus, implementation of this method for echo decorrelation mapping on a different imaging system may result in different optimal thresholds as predictors of specific ablation effects. Optimal thresholds for a modified imaging configuration could be determined by the ROC analysis reported here or by similar calibration procedures relating treatment severity to local echo decorrelation.

An important future step is in vivo testing of this echo decorrelation imaging method. The main challenge expected is possible spurious decorrelation caused by tissue motion. Notably, the echo decorrelation parameter defined by Equation 4 is insensitive to small signal phase changes, so that some tissue motion can be allowed without causing large artifacts. However, for robust clinical use, optimization of speed and motion sensitivity is important. In our experiments, echo data were acquired at the default frame rate (51 Hz) for the imaging transducer used. In an alternative implementation, local echo decorrelation could be mapped for echo signals separated in time by intervals of 100 microseconds or less, limited by the acoustic propagation time required for single lines, simi-

lar to data acquisition and processing in autocorrelation-based color Doppler imaging. Signal decorrelation during severe tissue heating may be substantial on such time scales compared with larger-scale tissue motion effects that occur on correspondingly larger time scales.

In conclusion, this work has shown that echo decorrelation imaging can map tissue changes due to RFA in vitro, and local echo decorrelation corresponds strongly with local tissue temperature elevations and ablation effects. Application of this method to clinical RFA monitoring will require further refinement of criteria for ablation detection, in vivo validation of echo decorrelation imaging, and further elucidation of the physical causes for this heat-induced ultrasound image phenomenon.

References

1. Curley SA. Radiofrequency ablation of malignant liver tumors. Ann Surg Oncol 2003; 10:338–347.
2. Erce C, Parks RW. Interstitial ablative techniques for hepatic tumours. Br J Surg 2003; 90:272–289.
3. Kudo M. Local ablation therapy for hepatocellular carcinoma: current status and future perspective. J. Gastroenterol 2004; 39:205–214.
4. Chiou SY, Liu JB, Needleman L. Current status of sonographically guided radiofrequency ablation techniques. J Ultrasound Med 2007; 26:487–499.
5. Leslie TA, Kennedy JE. High-intensity focused ultrasound principles, current uses, and potential for the future. Ultrasound Q 2006; 22:263–272.
6. Makin IRS, Mast TD, Faidi W, Runk MM, Barthe PG, Slayton MH. Miniaturized ultrasound arrays for interstitial ablation and imaging. Ultrasound Med Biol 2005; 31:1539–1550.
7. Buell J, Koffron A, Thomas M, Rudich S, Abecassis M, Woodle E, Laparoscopic liver resection. J Am Coll Surg 2005; 200:472–480.
8. Sanghvi NT, Fry FJ, Bihrle R, et al. Microbubbles during tissue treatment using high intensity focused ultrasound. Proc IEEE Ultrasonics Symp 1995; 2:1571–1574.
9. Rabkin BA, Zderic V, Crum LA, Vaezy S. Biological and physical mechanisms of HIFU-induced hyperecho in ultrasound images. Ultrasound Med Biol 2006; 32:1721–1729.
10. Dyson M. Non-thermal cellular effects of ultrasound. Br J Cancer Suppl 1982; 5:165–171.
11. Chen WS, Lafon C, Matula TJ, Vaezy S, Crum LA. Mechanisms of lesion formation in high intensity focused ultrasound therapy. Acoust Res Lett Online 2003; 4:41–46.
12. Jolesz FA, Hynynen K, McDannold N, Tempany C. MR imaging-controlled focused ultrasound ablation: a noninvasive image-guided surgery. Magn Reson Imaging Clin N Am 2005; 13:545–560.
13. Clasen S, Boss A, Schmidt D, et al. Magnetic resonance imaging for hepatic radiofrequency ablation [review]. Eur J Radiol 2006; 59:140–148.
14. Seip R, Ebbini ES. Noninvasive estimation of tissue temperature response to heating fields using diagnostic ultrasound. IEEE Trans Biomed Eng 1995; 42:828–839.
15. Varghese T, Zagzebski JA, Chen Q, et al. Ultrasound monitoring of temperature change during radiofrequency ablation: preliminary in-vivo results. Ultrasound Med Biol 2002; 28:321–329.
16. Righetti R, Kallel F, Stafford RJ, et al. Elastographic characterization of HIFU-induced lesions in canine livers. Ultrasound Med Biol 1999; 25:1099–1113.
17. Varghese T, Techavipoo U, Zagzebski JA, Lee FT. Impact of gas bubbles generated during interstitial ablation on elastographic depiction of in vitro thermal lesions. J Ultrasound Med 2004; 23:535–544.
18. Fahey BJ, Hsu SJ, Wolf PD, Nelson RC, Trahey GE. Liver ablation guidance with acoustic radiation force imaging: challenges and opportunities. Phys Med Biol 2006; 51: 3785–3808.
19. Lemor RM, Hoss M, Peter L, et al. Three dimensional ultrasonic monitoring of interstitial thermal tumor therapies: in vivo results. Proc IEEE Ultrasonics Symp 2003; 2:1284–1287.
20. Zhong H, Wan MX, Jiang YF, Wang SP. Monitoring imaging of lesions induced by high intensity focused ultrasound based on differential ultrasonic attenuation and integrated backscatter estimation. Ultrasound Med Biol 2007; 33:82–94.
21. Siebers S, Schwabe M, Scheipers U, Welp C, Werner J, Ermert H. Evaluation of ultrasonic texture and spectral parameters for coagulated tissue characterization. Proc IEEE Ultrasonics Symp 2004; 2:1804–1807.
22. Arthur RM, Straube WL, Trobaugh JW, Moros EG. Noninvasive estimation of hyperthermia temperatures with ultrasound. Int J Hyperthermia 2005; 21:589–600.
23. Hartley CJ, Ying H, Motomedi M. Ultrasonic Doppler detection of laser-tissue interaction. Ultrasound Med Biol 1994; 20:655–663.
24. Makin IRS, Mast TD, Faidi W, Runk MM, Barthe PG, Slayton MH. B-scan imaging and thermal lesion monitoring using miniaturized dual-functionality ultrasound arrays. Proc IEEE Ultrasonics Symp 2004; 2:1788–1791.
25. Kasai C, Namekawa K, Koyano A, Omoto R. Real-time two-dimensional blood flow imaging using an autocorrelation technique. IEEE Trans Sonics Ultrasonics 1985; 32: 458–464.

26. Li W, Lancée CT, Céspedes EI, van der Steen AFW, Bom N. Decorrelation of intravascular echo signals: potentials for blood velocity estimation. J Acoust Soc Am 1997; 102: 3785–3794.

27. Chen JF, Fowlkes JB, Carson PL, Rubin JM. Determination of scan-plane motion using speckle decorrelation: theoretical considerations and initial test. Int J Imag Syst Tech 1997; 8:38–44.

28. Kaluzynski K, Chen X, Emelianov SY, Skovoroda AR, O'Donnell M. Strain rate imaging using two-dimensional speckle tracking. IEEE Trans Ultrason Ferroelectr Freq Control 2001; 48:1111–1123.

29. Sun Z, Ying H, Lu J, Bell B, Cowan DF, Motamedi M. Automatic ultrasound determination of thermal coagulation front during laser tissue heating. IEEE Trans Ultrason Ferroelectr Freq Control 1999; 46:1134–1146.

30. O'Donnell M, Bauwens D, Mimbs JW, Miller JG. Broadband integrated backscatter: an approach to spatially localized tissue characterization in vivo. Proc IEEE Ultrasonics Symp 1979; 1:175–178.

31. Oppenheim AV, Schafer RW, Buck JR. Discrete-Time Signal Processing. Englewood Cliffs, NJ: Prentice-Hall; 1999.

32. Barthe PG, Slayton MH, Jaeger PM, et al. Ultrasound therapy system and ablation results utilizing miniature imaging/therapy arrays. Proc IEEE Ultrasonics Symp 2004; 2:1792–1795.

33. Thomsen SL. Qualitative and quantitative pathology of clinically relevant thermal lesions. Proc SPIE 2000; CR75:425–459.

34. Mast TD, Makin IRS, Faidi W, Runk MM, Barthe PG, Slayton MH. Bulk ablation of soft tissue with intense ultrasound: modeling and experiments. J Acoust Soc Am 2005; 118: 2715–2724.

35. Anand A, Byrd L, Kaczkowski PJ. In situ thermal parameter estimation for HIFU therapy planning and treatment monitoring. Proc IEEE Ultrasonics Symp 2004; 1:137–140.

36. Mast TD, Salgaonkar VA, Karunakaran C, Besse JA, Datta S, Holland CK. Acoustic emissions during 3.1 MHz ultrasound bulk ablation in vitro. Ultrasound Med Biol 2008; 34:1434–1448.

37. Damianou CA, Sanghvi NT, Fry FJ, Maass-Moreno R, Dependence of ultrasonic attenuation and absorption in dog soft tissues on temperature and thermal dose. J Acoust Soc Am 1997; 102:628–634.